1 # A 3D Full Stress Tensor Model for Oklahoma

2 **Enter authors here: Chengping Chai[1], Andrew A. Delorey[2], Monica Maceira[3], Will**

3 **Levandowski[4], Robert A. Guyer[2], Haijiang Zhang[5], David Coblentz[2], and Paul A. Johnson[2]**

4 [1]Oak Ridge National Laboratory, Oak Ridge, Tennessee 37830, U.S.A.

5 [2]Los Alamos National Laboratory, Los Alamos, New Mexico 87545, U.S.A.

6 [3]Department of Physics and Astronomy, University of Tennessee, Knoxville, Tennessee 37996,

7 U.S.A.

8 [4]Colorado College, Colorado Springs, Colorado 80903, U.S.A.

9 [5]School of Earth and Space Sciences, University of Science and Technology of China, Hefei,

10 Anhui 230026, China.

11 Corresponding author: Chengping Chai (chaic@ornl.gov) and Andrew A. Delorey

12 (andrew.delorey@lanl.gov)

13 **Key Points:**

14 - We compute the stress field using finite element modeling by considering contributions

15   from both gravitational and far-field tectonic forces

16 - The simulated stress field in Oklahoma agrees with observed stress indicators including

17   the orientation of S_{Hmax} and the faulting type

18 - Gravitational contribution to the horizontal stress field has a comparable magnitude

19   regarding tectonic contribution for the upper 5 km

20

Abstract

The stress tensor is an important property for upper crustal studies such as those that involve

pore fluids and earthquake hazards. At tectonic plate scale, plate boundary forces and mantle

convection are the primary drivers of the stress field. In many local settings (10s to 100s of km

and <10 km depth) in tectonic plate interiors, we can simplify by assuming a constant

background stress field that is perturbed by local heterogeneity in density and elasticity. Local

stress orientation and sometimes magnitude can be estimated from earthquake and borehole-

based observations when available. Modeling of the local stress field often involves

interpolating sparse observations. We present a new method to estimate the 3D stress field in the

upper crust and demonstrate it for Oklahoma. We created a 3D material model by inverting

multiple types of geophysical observations simultaneously. Integrating surface-wave dispersion,

local travel times and gravity observations produces a model of P-wave velocity, S-wave

velocity and density. The stress field can then be modeled using finite element simulations. The

simulations are performed using our simplified view of the local stress field as the sum of a

constant background stress field that is perturbed by local density and elasticity heterogeneity

and gravitational body forces. An orientation of N82˚E, for the maximum compressive tectonic

force, best agrees with previously observed stress orientations and faulting types in Oklahoma.

The gravitational contribution of the horizontal stress field has a magnitude comparable to the

tectonic contribution for the upper 5 km of the subsurface.

1 Introduction

The stress tensor is an important geophysical property of the subsurface and is highly

important to tectonic and earthquake studies (e.g., Heidbach et al., 2018; Levandowski et al.,

2016, 2018; McGarr & Gay, 1978; M. L. Zoback & Magee, 1991; M. Lou Zoback & Zoback,

44   1980) and subsurface engineering (Liu et al., 2017; Martínez-Garzón et al., 2013; Nussbaum et

45   al., 2017; M. D. Zoback et al., 2010). Principal stress orientations (sometimes with magnitude)

46   have been modeled or observed at tectonic plate scales in the World Stress Map (Heidbach et al.,

47   2018). Orientations of maximum horizontal principal stress (S_{Hmax}) are typically determined

48   using borehole and surface techniques (Lin et al., 2018; Ljunggren et al., 2003) and

49   heterogeneity likely exists at all scales (Hsu et al., 2010; Iio et al., 2017; Lund Snee & Zoback,

50   2016; Rivera & Kanamori, 2002; Schoenball & Davatzes, 2017). Below the deepest available

51   stress measurements, much of what we know of shear stress magnitudes on faults is from stress

52   rotations associated with large earthquakes as measured with focal mechanisms (see Hardebeck

53   & Okada, 2018 and references therein). The World Stress Map (Heidbach et al., 2018) catalogs

54   tens of thousands of orientations of the S_{Hmax}, some of which are associated with information on

55   the style of faulting (e.g., normal, strike-slip, or reverse). The full stress tensor, including

56   principal component magnitudes, is largely unknown away from boreholes and earthquakes.

57   Contributions from quasi-static forces to the stress tensor at any point in the Earth's upper

58   crust in order of magnitude are (1) gravitational body forces (0-100s of MPa, increasing with

59   depth), (2) tectonic (plate boundary and bottom tractions, 10s of MPa or more, (Richardson et al.,

60   1979), and (3) local, related to slip on faults (~10 MPa or less) and poroelastic stress (< 2 MPa)

61   (Segall, 1989). Stress changes due to recent slip on faults can be locally significant but are

62   limited in spatial extent except for those associated with very large earthquakes (Wesson &

63   Boyd, 2007). These forces act on subsurface structures with heterogeneous elastic properties,

64   resulting in a heterogeneous stress field. Published continental and regional stress modeling

65   results (e.g., Fleitout & Froidevaux, 1982; Flesch et al., 2000, 2007; Forte et al., 2007; Ghosh et

66   al., 2013, 2019; Humphreys & Coblentz, 2007; Levandowski et al., 2016; Liu et al., 2017; Reiter

67 & Heidbach, 2014) have been used to explain large-scale deformations (e.g. mountain building)

68 and seismicity (both interplate and intraplate). The importance of the gravitational contribution

69 in stress modeling has been emphasized by Humphreys & Coblentz (2007) and Flesch et al. (

70 2000, 2007). Forte et al. (2007) and Levandowski et al. (2016) suggest both tectonic forces and

71 subsurface elastic property heterogeneity may have contributed to the seismicity of the New

72 Madrid seismic zone. Flesch et al. (2007) found that the gravitational potential energy and

73 tectonic forces contribute to the deviatoric stress magnitude almost equally in western North

74 America. However, it is not clear whether the gravitational and tectonic contributions are similar

75 to the deviatoric stress magnitude in other regions. We chose the Oklahoma area to study the 3D

76 stress field variations since previously published stress observations in the area can validate our

77 stress modeling method. We hypothesize that most of the observed deviations from the tectonic

78 stress field in Oklahoma are due to gravitational effects and heterogeneity in material properties

79 including density and elastic modulus. By modeling both the gravitational and tectonic

80 components of the stress field, we can both test this hypothesis and constrain principal

81 component magnitudes. For the purposes of this paper, "tectonic" stress refers to stresses that are

82 imparted on our study area through boundary conditions and includes such things as ridge push,

83 slab pull, and basal traction. More detailed material models have been suggested as one approach

84 to improve stress models by several researchers (e.g., Ghosh et al., 2019; Reiter & Heidbach,

85 2014). In order to model the gravitational and tectonic components of the stress field in

86 Oklahoma accurately, we require a detailed 3D material model and information (direction and

87 magnitude) about tectonic forces. Since directions and magnitude of tectonic forces are not

88 known for most regions, we estimate them with stress observations via multiple stress modeling

89 tests. The material model can be obtained from subsurface seismic structure investigations.

90   A few detailed investigations have focused on the 3D crustal structure in the Oklahoma

91   region. Evanzia et al. (2014) studied the upper mantle structure using teleseismic body wave

92   tomography in the Texas and Oklahoma area. A few regional and continental scale studies

93   mainly based on Earthscope Transportable Array data with nominal station spacing of ~70 km

94   (e.g., Chai et al., 2015; Porter et al., 2016; Schmandt et al., 2015; Shen & Ritzwoller, 2016)

95   imaged the broad-scale structure of the Oklahoma region. Limited by different scope and focus

96   of these studies, fine scale subsurface structure of both P- and S-wave velocities in the study area

97   is not well resolved. Seismic velocity models produced by these broader scale studies can be

98   used as a starting model for more detailed investigations. The compiled global model Crust 1.0

99   (Laske et al., 2013) was produced by combining Earth models from active source surveys.

100   However, the coverage and resolution of these earlier studies are not sufficient for our stress

101   modeling. We constructed a material model to extend these earlier efforts.

102   In this paper, we first present data used in our technique that includes observations for

103   material model inversion and for stress modeling. Details on the inversion for the material model

104   and stress modeling are documented in the following section. Then, we present results for the

105   material model and the stress model of the Oklahoma region. The major findings, assumptions,
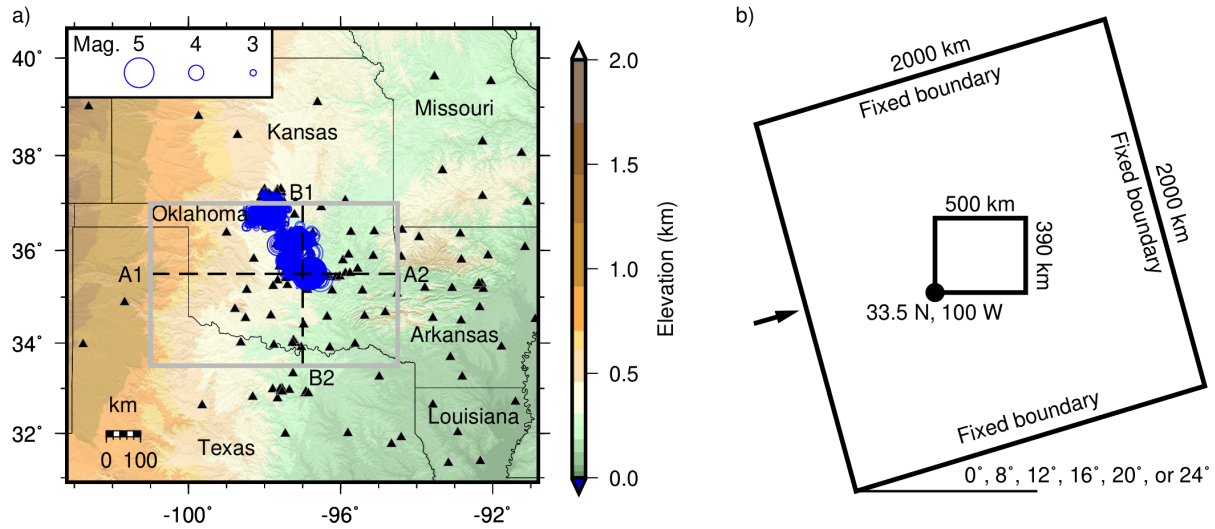
106   and limitations are discussed in the last section.

107   **2 Data**

108   Our analysis consists of constraining a material model (P- and S-wave velocity and

109   density) and stress modeling, which requires both geophysical observations and stress

110   measurements.

111   2.1 Observations for material model inversion

112   We simultaneously and jointly invert local P- and S-wave first arrival times, Rayleigh-

113   wave and Love-wave dispersion maps, and satellite-derived Bouguer gravity observations to

114   model the 3D subsurface P- and S-wave velocity and density structure. Each of these datasets

115   went through various quality control procedures. Interactive visualization tools (Chai et al.,

116   2018) were used to visually examine the datasets as well as the resulting material models. Details

117   of the data selection and preprocessing are documented in the following paragraphs.

118   The local body waves arrival time dataset (catalog locations and P- and S- arrivals) was

119   obtained from United States Geological Survey (McNamara et al., 2015). Catalog arrival times

120   that we suspected to be erroneous, such as those leading to more than 5 s misfits (unrealistically

121   large), were excluded from the inversion for material properties. Only events with 6 or more P-

122   wave arrival times are included in the inversion so the location of seismic events is well

123   constrained. The final arrival times dataset used in the inversion comprises 58,896 P-wave

124   arrivals and 20,155 S-wave arrivals from 3,740 earthquakes that were recorded at 157 seismic

125   stations between November 2011 and July 2015 (Figure 1a). Besides absolute catalog body wave

126   arrival times, differential catalog times were computed (Waldhauser, 2000) and included in the

127   inversion (Zhang & Thurber, 2003) because of their ability to further improve the relative

128   locations of neighboring earthquakes and their surrounding velocities. As shown in Figure 1,

129   most of the earthquakes are located in north central Oklahoma, and the station distribution is

130   reasonable with a good azimuthal coverage.

Figure 1. Study area map (a) and the finite element model design (b). The map shows the location of seismic events (blue open circles) and stations (black solid triangles) used to construct the body wave arrival time dataset. The size of the circles is a function of magnitude. The dashed lines indicate locations of the cross-sections in Figure 7. The gray box shows the area for Figure 6. The finite element model is a hexahedron with sides 2000 km long and depth of 200 km. The axes of the full model are aligned with the tested tectonic force directions in Figure 8. The axes of the rectangle bounding the study area are aligned west-east and south-north. The geographic origin of the study area is noted on the figure. The arrow indicates direction of displacements applied on the southwest boundary to produce a maximum horizontal compressive stress oriented southwest to northeast.

The surface wave dispersion estimates (used as observations in this study) were obtained

from an update of Herrmann et al. (2016). The dispersion model was constrained with local

earthquake and ambient noise measurements. Group and phase velocities of both Rayleigh and

Love waves are available online (Herrmann et al., 2016). We use periods ranging from 5.0 s to

51.5 s with 24 data points per dispersion curve when sufficient data are available. The surface

wave data were resampled from the dispersion model onto a 0.5˚ by 0.5˚ horizontal grid that

covers the study area. Four dispersion curves at each of these horizontal grid nodes are included

in the inversion when available. The Bouguer gravity data (observations for this study) was

extracted from the global model WGM2012 (Balmino et al., 2012) and sampled to the same

horizontal grid as for the dispersion observations. The gravity data was filtered in the wavelength

domain to avoid overfitting and to remove long-wavelength features mainly caused by deep

153   density variations. Very short wavelength (less than 50 km) and long wavelength (longer than

154   200 km) anomalies were excluded since they are beyond our spatial resolution (50 km laterally).

155   Gravity observations at the four edges (around 200 km wide) were not used in the inversion to

156   avoid edge effects (no gravity contributions outside of the study area). We used a larger area (the

157   entire region as shown in Figure 1a) for the velocity model inversion so that the edge effects do

158   not influence our results.

159   2.2 Observations for stress modeling

160   During the stress modeling, we used S_{Hmax} orientations and A_ϕ (Simpson, 1997) as data

161   constraints. A total of 94 S_{Hmax} orientations with uncertainties of 15°, 20° or 25° referred

162   respectively as qualities A, B, and C (Heidbach et al., 2018) were accepted as stress

163   observations. A_ϕ (Simpson, 1997) is determined from the magnitudes of the 3 principal stresses

164   and ranges from 0 (radial extension) to 3 (radial constriction), where the values for pure normal,

165   pure strike-slip, and pure reverse are 0.5, 1.5, and 2.5, respectively. We used A_ϕ values from

166   (Levandowski et al., 2018) in our stress inversion because they cover our study area and have

167   published uncertainties, though other interpretations exist (Lund Snee & Zoback, 2016).

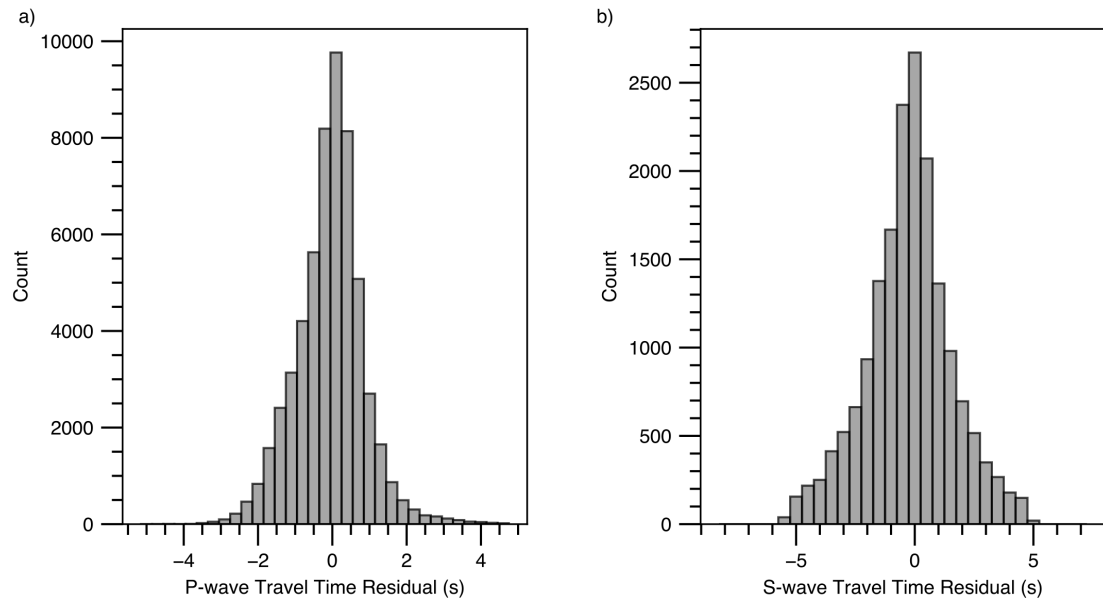168   **3 Method**

169   We first describe the approach that we used to obtain the material model. Then, we

170   document details on the stress modeling.

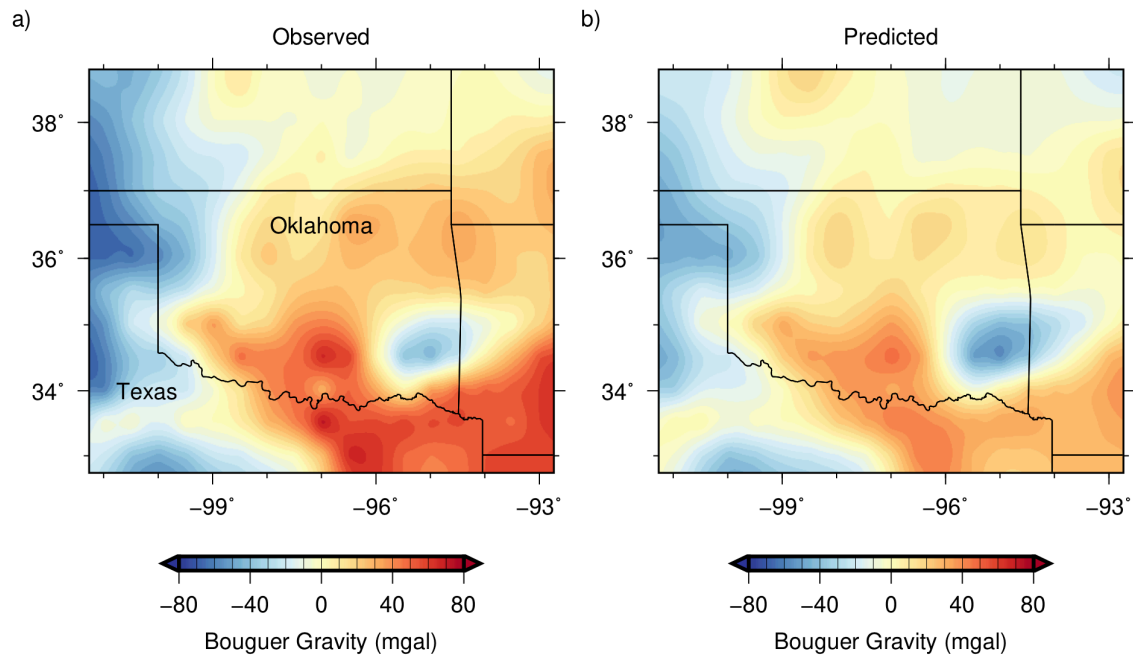171   3.1 Inversion for the material model

172   The joint inversion technique we used is the same as that of Syracuse et al. (2016, 2017)

173   which used multiple geophysical datasets to directly constrain P- and S-wave velocities, and
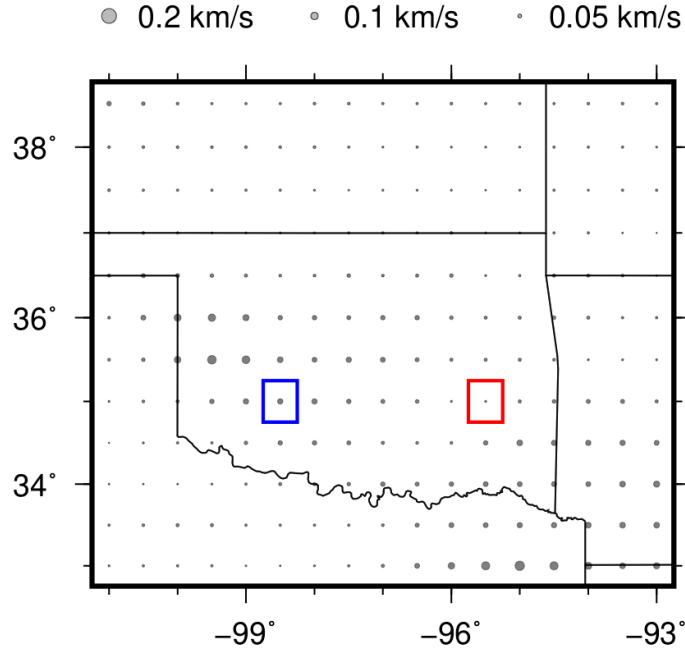
174 mass density. The inversion algorithm was developed based on tomoDD (Zhang & Thurber,

175 2003, 2006) and an inversion program that simultaneously inverts surface-wave and gravity data

176 (Maceira & Ammon, 2009). The shear velocity-density relationship from Maceira & Ammon

177 (2009) was used to relate gravity observations to seismic speeds. We started the inversion using a

178 3D initial model from Chai (2017), which was constrained with spatially smoothed P-wave

179 receiver functions (Chai et al., 2015), surface-wave dispersion (Herrmann et al., 2016) and

180 gravity observations (Balmino et al., 2012). The inversion iteratively updated the P- and S-wave

181 velocity models by minimizing the data fits and taking into consideration other regularizations

182 constraints such as smoothing and damping. Different weights were assigned to each type of data

183 constraints. We performed two suites of inversions to find the optimal combination of weights

184 using L-curve analysis as suggested by Syracuse et al. (2015). The first set of inversions

185 searched for the appropriate damping and smoothing values (see Figure S1 and Visualization S1

186 in the electronic supplements). The second set explored the weights for gravity and surface-wave

187 data (see Figure S2 and Visualization S2 in the electronic supplements). The optimal material

188 model (P- and S-wave velocities and density) was selected by minimizing an objective function

189 of data fits and regularization terms similar to Syracuse et al. (2016, 2017). The optimal material

190 model fitted the travel times (Figure 2), gravity observations (Figure 3), and surface-wave

191 dispersions (Figure 4-5 and Figure S3) reasonably well. Earthquake locations were updated

192 during the inversion simultaneously as well.

193

Figure 2. Histograms showing P- (a) and S- (b) wave travel time residuals associated with the inversion of the material model.

Figure 3. A comparison of (a) the observed Bouguer gravity and (b) the predicted gravity for the inversion of the material model.
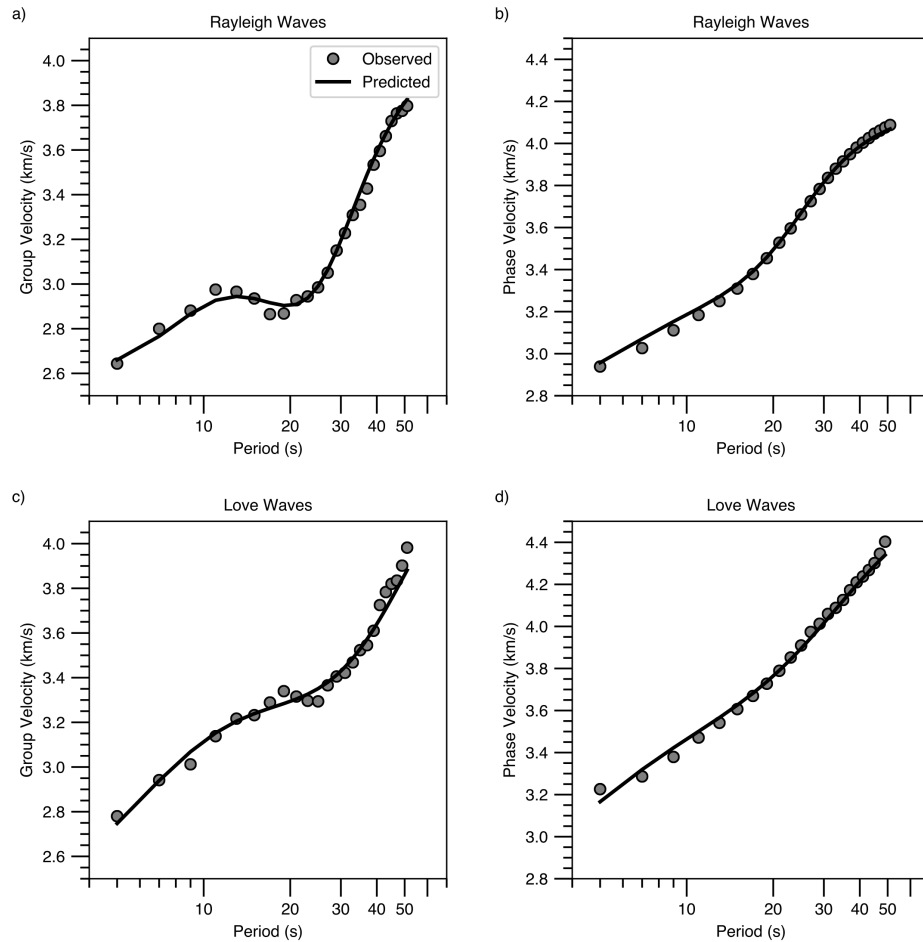
Figure 4. A map showing misfits between surface-wave dispersion observations and predictions with the optimal material model. Smaller dots indicate lower misfits. The red box indicates the location of the data showing in Figure 5. The blue box shows the location of the data showing in Figure S3. The largest misfit is 0.13 km/s. The minimum misfit is 0.02 km/s.

3.2 Stress modeling

We used a commercial finite element code (ABAQUS standard/implicit, version 2018) to

model both the tectonic and gravitational body force components of the stress field. The full

finite element model is 2000 km along each horizontal dimension and 200 km in depth (Figure

1b). The model was designed to accurately represent stress in the uppermost crust (<10 km), and

we do not interpret any results for the deeper crust or upper mantle. Our study area, which falls

geographically within 33.5 to 37.0 N latitude and 100 to 94.5 W longitude and is approximately

390 km south to north and 500 km west to east, is centrally embedded within the full model. The

axes of this central part of the model were oriented west-east and south-north while the full

model was rotated by 0°, 8°, 12°, 16°, 20°, or 24° counterclockwise to correspond to the

principal orientations of the modeled tectonic stress field. These directions correspond to

azimuths of N90°E, N82°E, N78°E, N74°E, N70°E, and N66°E, respectively, mimicking the

219   general ENE-WSW S_{Hmax} orientations in central and eastern North America (Alt & Zoback,

220   2017; Heidbach et al., 2018; Levandowski et al., 2018; Walsh & Zoback, 2016). The source of

221   this regional stress field is not the focus of this study, but such directions closely accord with

222   either Mid-Atlantic Ridge push or basal drag of North American absolute motion (M. Lou

223   Zoback & Zoback, 1980).

Figure 5. Examples of observed and predicted dispersion curves for an example grid point
shown in Figure 4, a) Rayleigh wave group velocities, b) Rayleigh wave phase velocities, c)
Love wave group velocities, d) Love wave phase velocities.

229   The finite elements are 8 node hex, elastic elements with horizontal dimensions of 12 km

230   by 12 km and vertical dimensions of 2 km near the surface, increasing to 20 km vertical spacing

231   near the base. The material properties (P- and S-wave velocities, and density) from the joint

12

232   inversion were mapped to the geographically appropriate elements. Elements that fall outside the

233   boundaries of our material model were assigned the median value for their depth. We converted

234   the P- and S-wave velocities, and density into Young's modulus and Poisson's ratio (input for

235   ABAQUS) using formulas from Shearer (2009). The formulas are also included in Text S1.

236   We modeled the effect of body forces (gravity) by holding constant normal displacement

237   boundary conditions on the four sides and bottom and then apply the gravitational field. This

238   process was performed using a "geostatic" step in ABAQUS. Normally, a volume with body

239   forces applied and zero normal displacement boundary conditions on the bottom and all

240   horizontal boundaries would compress under its own weight. In this geostatic procedure, we

241   determined equilibrium stress conditions for the model due to the applied body forces and

242   boundary conditions, while maintaining the original dimensions. With this procedure, we began

243   with a model that is pre-stressed with overburden before we apply tectonic stress. The

244   overburden stress is approximately the product of density and gravitational acceleration

245   integrated over the depth. Due to 3D heterogeneity in density and elasticity, the stress field

246   caused by overburden is also heterogeneous.

247   We modeled tectonic stress by imposing a small, uniform (inward) displacement of 61 m

248   along the southwest facing boundary of the full model and zero displacement boundary

249   conditions on the northwest, southeast, and northeast sides (Figure 1b). The displacement applied

250   is approximately equivalent to a tangential compressional stress of 1.9 MPa in the direction of

251   the displacement in the upper 5 km. Since the elastic model is linear, we increment the resulting

252   stress field to model different tectonic stress magnitudes. We intend the applied boundary

253   conditions to approximate any regional contributions to the stress field including plate boundary

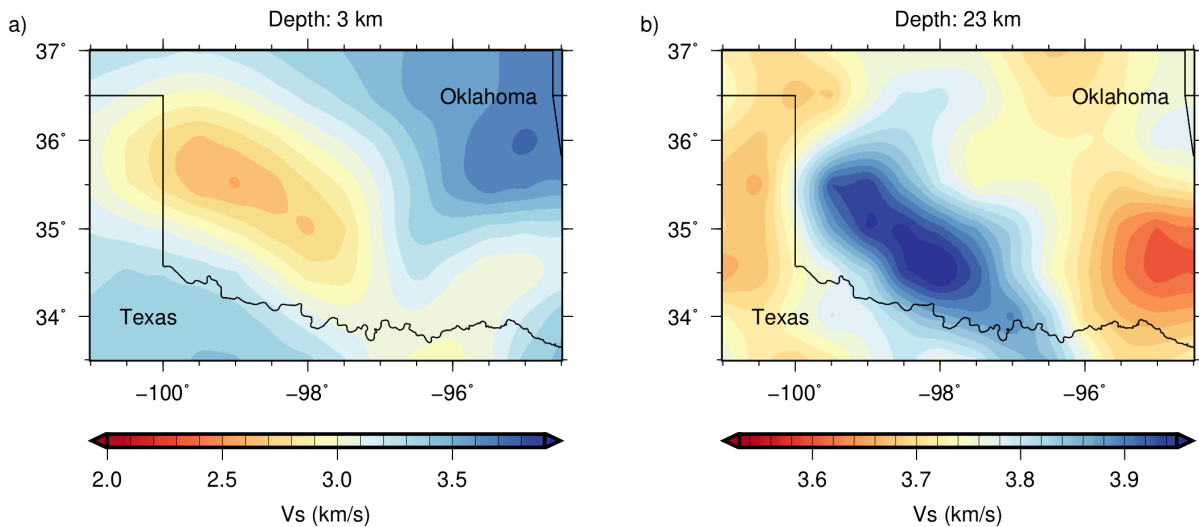254   forces and uniform tractions at the bottom of the lithosphere.

255   We determined the magnitude of the tectonic force for the best overall fit to the available

256 stress measurements. The depth of measured S_{Hmax} orientations varies, with those derived from

257 borehole measurements at 1 km or more and earthquake moment tensor solutions at 4-5 km. To

258 determine fit to S_{Hmax} orientations, we compared the modeled S_{Hmax} orientations with observed

259 S_{Hmax} orientations (Figure 9). We also used faulting type as a constraint because faulting type is

260 determined by the relative magnitudes of the principal stresses (e.g., Simpson, 1997). In our

261 study area, the dominant style of faulting is strike-slip (Dziewonski et al., 1981), but there are

262 significant and spatially variable amounts of net horizontal extension accommodated by oblique-

263 normal and normal faulting (Levandowski et al., 2018; Walsh & Zoback, 2016).

264   Using the orientation of 94 available stress indicators (S_{Hmax}) and the faulting types in

265 Oklahoma, we search for the orientation and magnitude of the tectonic force by finding the

266 model that best fits the stress observations. When both the magnitude and orientation of S_{Hmax} are

267 available, alternative approaches (Reiter & Heidbach, 2014) can also be used to determine the

268 orientation and magnitude of the tectonic force. We calculated all plausible magnitudes for a set

269 of orientations and identified the best magnitude and orientation of the tectonic force by

270 minimizing the following function

271              $(\boldsymbol{G}m - d)^T \boldsymbol{C}_d^{-1}$ (1)

272   where $\boldsymbol{G}$ is the Jacobian matrix describing the relationship between the model parameters

273 and the model predictions, m is model vector, $\boldsymbol{C}_d$ are the reported data uncertainties, and d is the

274 data vector. The model vector has two values, the tectonic force magnitude and orientation. The

275 data vector is composed of observed stress orientations (S_{Hmax}), and A_ϕ. The misfit of each

276 prediction is scaled by the uncertainty of the underlying observation using $\boldsymbol{C}_d$. S_{Hmax} is a measure

277 of the relative magnitudes of the two horizontal principal stresses, while A_ϕ is a measure of the

278   relative magnitudes of all three principal stresses. Combining these two types of stress

279   observations provide constraints on both the direction and magnitude of the tectonic force.

280

281   **Figure 6**. Depth slices of the shear velocity model at 3 (a) and 23 (b) km. The corresponding
282   color scale is shown beneath the depth slice. The black line is the state boundary between
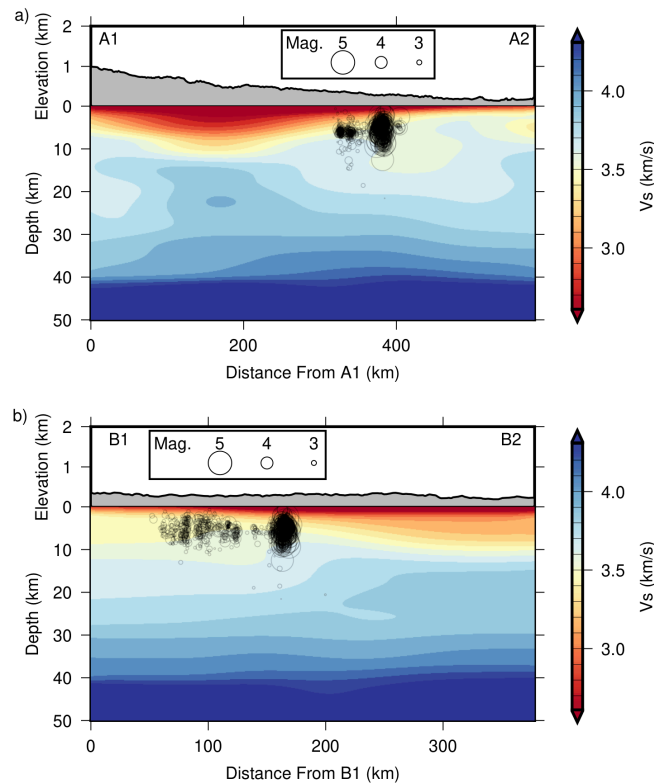283   Oklahoma and Texas.

284   **4 Results**

285   Our results include a 3D material model and a 3D stress model.

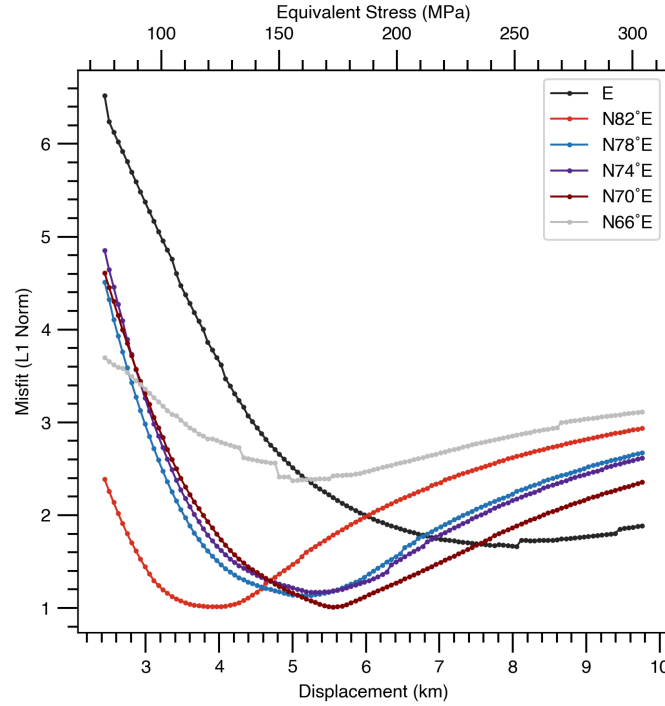286   4.1 Material model

287   We use depth slices, cross-sections, and interactive visualization to present the 3D

288   material model. Depth slices and two cross-sections of the S-wave velocity model are shown in

289   Figure 6 and 7, respectively. Depth slices of the P-wave velocity and density models are shown

290   in Figure S3, and S4 in the electronic supplements, respectively. An interactive tool (Chai et al.,

291   2018) is provided in the electronic supplements (Figure S5 and Visualization S3) to view the

292   seismic velocities at other locations in the model. Our material model confirms previous

293   geophysical and geological surveys but with a more complete image. At 3 km depth (Figure 6),

294   the slow anomaly in southwest Oklahoma corresponds to the Anadarko basin. The anomaly

extends more than 10 km in depth as we can see in the cross-section A1-A2 (Figure 7), which

agrees with Johnson's geological compilation (Johnson, 2008). Low seismic velocities (upper 10

km in Figure 7) are likely associated with the Anadarko basin. The relative location between the

imaged low velocities and the majority of the earthquakes is consistent with Isken & Mooney

(2017)'s results. In the mid and lower crust (~15-40 km in depth), we image a high-velocity

anomaly beneath the Anadarko basin. The high-velocity anomaly may be related to the past

igneous activity associated with the Southern Oklahoma Aulacogen (Gilbert, 1983). We found a

slower upper mantle beneath the southern Oklahoma that is consistent with Evanzia et al.

(2014)'s model.

Figure 7. Cross-sections A1-A2 (a) and B1-B2 (b) of the shear velocity model. Locations of the
cross-sections are shown in Figure 1. The black circles indicate the refined earthquake locations.

16

308

Figure 8. A comparison of misfits of stress indicators and faulting type for five different tectonic
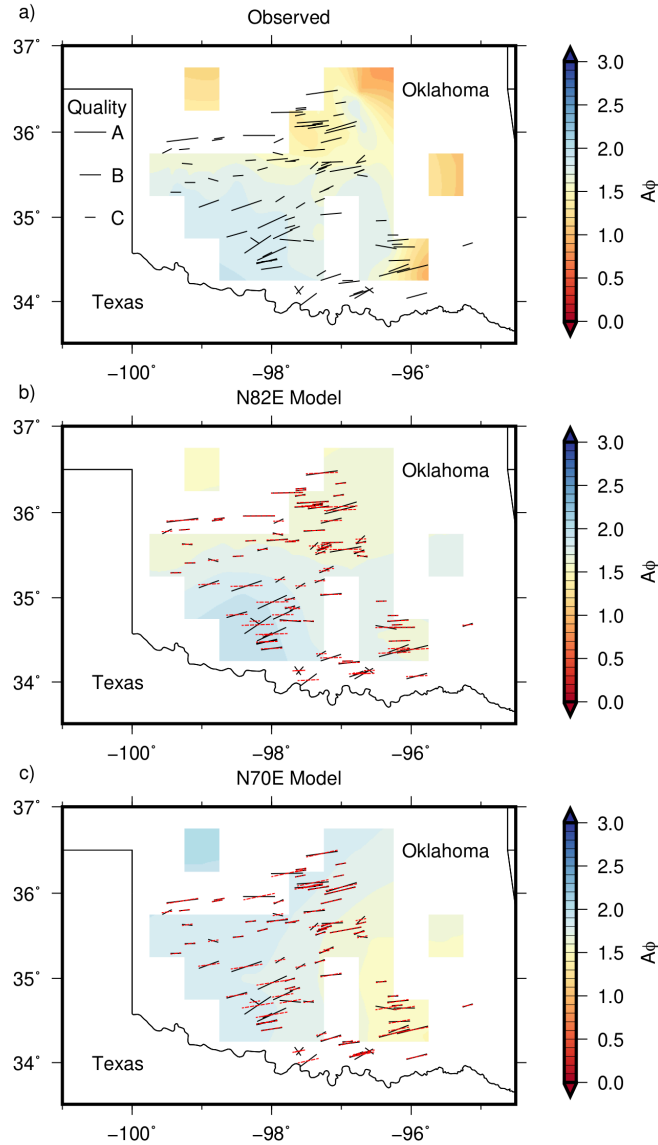orientations as a function of magnitude of tectonic force.

311   4.2 Stress model

312   The orientation of the maximum horizontal principal stress (S_{Hmax}) for majority of the

313   stress indicators varies between East and N60˚E. In an attempt to constraint the orientation of the

314   tectonic forces applied to our model, the misfit between the observed and predicted stress

315   orientation was evaluated for a range of boundary force orientations which represent the far-field

316   tectonic forces (Figure 8). For all the cases considered, the misfit is high for very low magnitudes

317   of tectonic force (displacements < 3 km).   We interpret this high misfit as a consequence of

318   gravitational body forces dominating the calculated stresses. Conversely, the high misfit for very

319   high tectonic forces (displacements >7 km) is the consequence of tectonic stresses dominating

320   the predicted stress orientations. For most of the cases considered the misfit is minimized for

321   tectonic stresses imparted by a range of ~4 to ~6 km displacement. For orientations in the range

322   of E-N66˚E, the two best fits are models with a displacement of 3965 m (~123 MPa) with an

17

323   orientation of N82ºE and a displacement of 5551 m (~173 MPa) with an orientation of N70ºE.

324   These two models have a nearly identical overall misfit and this bimodal misfit surface is due to

325   the interplay between S_{Hmax} and A_ϕ (Figure 8). The N82ºE model fits the spatial variations of the

326   observed A_ϕ a little better than the observed S_{Hmax} directions (Figure 9). Compared to the N82ºE

327   model, the N70ºE model fits the observed S_{Hmax} directions equally well, but not as well for the

328   observed A_ϕ (Figure 9). For this reason, we choose the N82ºE model as our preferred model.

329   Higher displacements produce models more towards reverse faulting and a more spatially

330   uniform orientation for predicted S_{Hmax}, and lower values produce a model more towards normal

331   faulting and more variable spatial orientations for predicted S_{Hmax}. An arbitrarily high tectonic

332   force is not supported by the data both in terms of the orientation of S_{Hmax} and the faulting type

333   for the best fitting stress orientations (Figure 8). The best fitting model, that does not consider

334   gravitational body forces, is for a stress orientation of N66ºE with an arbitrary displacement

335   magnitude, and has a normalized misfit of 3.85 compared to 1.01 for our preferred model (Eq.

336   1). This means that stress caused by gravitational body forces explains most of the residual

337   misfit of a uniform model, supporting our hypothesis.

338   According to previous studies, A_ϕ ranges from ~1.0 in northernmost Oklahoma to 1.5 in

339   central and southern Oklahoma (Levandowski et al., 2018; Lund Snee & Zoback, 2016; Walsh &

340   Zoback, 2016). Though poorly constrained by focal mechanism inversions, portions of southern

341   Oklahoma may have A_ϕ of up to 1.7 (Levandowski et al., 2018; Lund Snee & Zoback, 2016). A_ϕ

342   of the N82°E stress model falls within the range for strike slip faulting with some regions in the

343   southwest having higher values. The models with a tectonic force orientation of E and N66˚E

344   have considerably higher misfits to the weighted sum of S_{Hmax} and A_ϕ (Figure 9). The resulting

345   stress field has a S_{Hmax} orientation from southwest to northeast, consistent with average S_{Hmax}

18

346 measurements (Alt & Zoback, 2017; Heidbach et al., 2018) and focal mechanism inversions

347 (Levandowski et al., 2018; Walsh & Zoback, 2016). The deviatoric shear stress associated with

348 these stress magnitudes are in the range of 10 to 30 MPa on optimally oriented faults at

349 earthquake depths. The stress orientations and deviatoric stress magnitudes predicted here are

350 consistent with the intraplate stress field predicted in Oklahoma (Alt & Zoback, 2017) and mid-

351 plate North America as described in a number of previous studies; including qualitative

352 assessments of the states of stress (e.g., M. Lou Zoback, 1992; M. Lou Zoback & Zoback, 1980),

353 numerical models of the intraplate stress field using whole-plate linear elastic shell models (e.g.,

354 Humphreys & Coblentz, 2007; Richardson & Reding, 1991), as well as more recent evaluations

355 of the relative stress magnitudes and orientations (Heidbach et al., 2007, 2010, 2018; Lund Snee

356 & Zoback, 2020). While the orientation of the S_{Hmax} for the intraplate stress field is farily well-

357 constrained and understood in the context of local heterogeneities (see discussion in Schoenball

358 & Davatzes, 2017), the magnitude of the intraplate stress field remains more elusive. The stress

359 magnitudes predicted here are consistent with the body of evidence that the tectonic stresses in

360 the lithosphere are generally of the order of tens of MPa averaged over the thickness of the

361 lithosphere.

362

Figure 9. (a) Stress observations and modeled results using a displacement of (b) 3965 m (the orientation of the tectonic force is N82˚E) and (c) 5551 m (the orientation of the tectonic force is N70˚E). Black lines are observed orientations of S_{Hmax} from Alt & Zoback (2017) and Heidbach et al. (2018). Red dashed lines represent the modeled S_{Hmax} orientations. The length of the lines indicates the quality of the observations. The background shows A_ϕ (Simpson, 1997) values computed from the stress model. A_ϕ value of 1.5 corresponds to strike-slip faulting. As A_ϕ values increase from 1.5, the faulting type evolves towards reverse faulting and as values decrease from 1.5 faulting type evolves towards normal faulting.
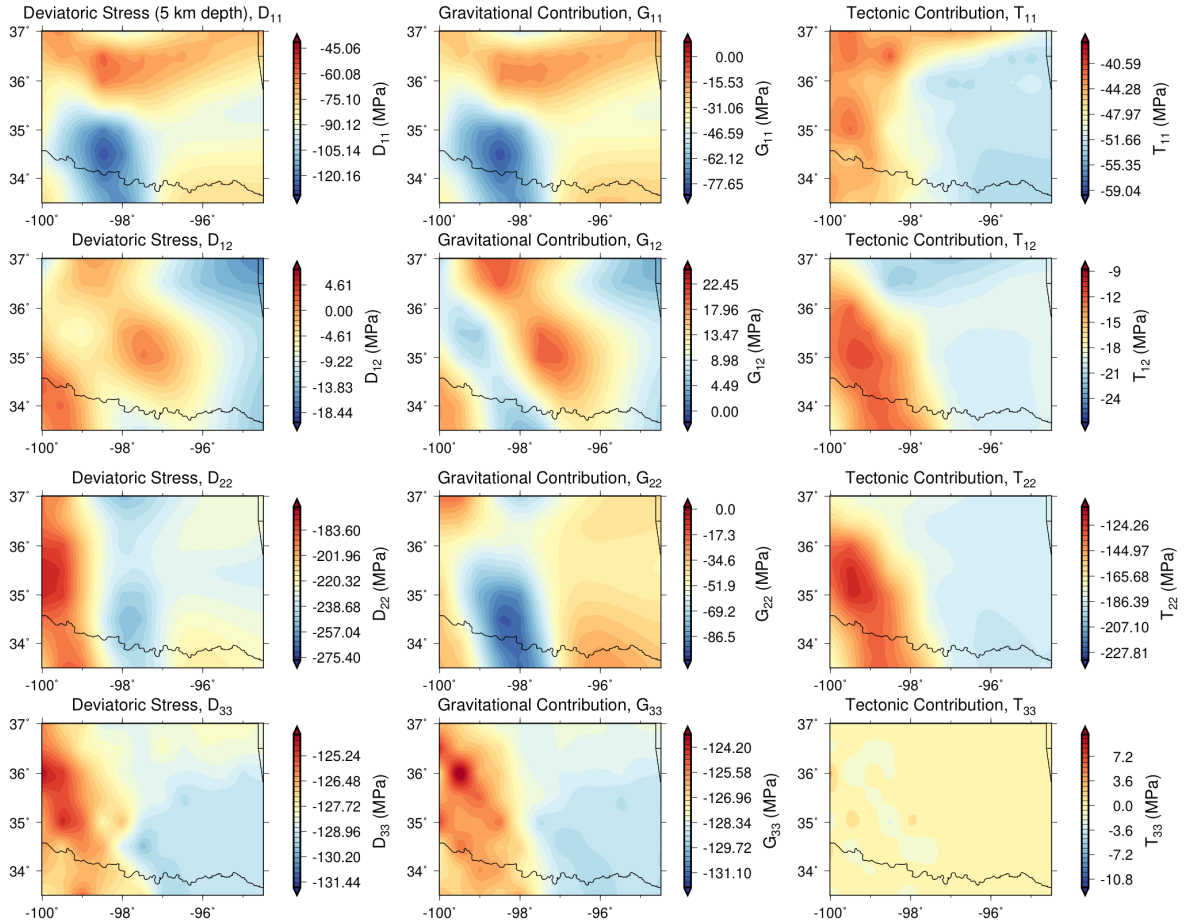
371

Figure 10. A comparison of magnitudes of deviatoric stress (left column) and its gravitational (middle column) and tectonic contributions (right column) at 5 km depth using the preferred stress model. The color scale changes for each image. The deviatoric stress tensor D is the sum of the gravitational contribution G and the tectonic contribution T. The first subscript is the orientation of the surface that the tensor component acts on. The second subscript of the tensor component is the direction of component. Subscript 1 represents north, 2 for east, and 3 for down.

We examine the stress field at the 5 km depth for the Oklahoma area. Comparing the horizontal component of the gravitational contribution with the tectonic contributions (Figure 10), we found the gravitational contributions to the horizontal components of the deviatoric stress field (subtracting out the hydrostatic stress) is on the same order of magnitude to the tectonic contribution. The vertical component of the stress field is dominated by the gravitational contribution. Due to spatial changes in density and elastic properties, both the gravitational

386   contributions and the tectonic contributions are non-uniform for the horizontal components. The

387   spatial distributions of gravitational and tectonic contributions show different patterns. The

388   resulting modeled deviatoric stress field shows spatial variability across Oklahoma. As a result,

389   we need to include both the gravitational and tectonic contributions in the stress field calculation,

390   which confirms previous studies for other regions (e.g., Levandowski et al., 2016; Reiter &

391   Heidbach, 2014). The tectonic contribution to stress on optimally oriented faults is between 10-

392   30 MPa within the study area; the gravitational contribution is 0-20 MPa, mostly of opposite

393   sign, but of similar magnitude.

394   We acknowledge that tectonic forces acting on the study area through the boundaries are

395   almost certainly not uniform in the Earth. But a uniform force at the boundaries is sufficient for

396   testing the hypothesis that variations from a uniform stress field in the upper crust are primarily

397   due to heterogeneous elasticity and density in the crust at local and regional scales. As our model

398   is fully elastic, we are also neglecting the effect of viscoelastic behavior in the lower crust and

399   upper mantle, which would have the effect of relaxing stresses at those depths with some time

400   dependence. Our intent in this study is to present a method to model stresses in the upper crust

401   where earthquakes and other activities occur, not calculate a stress model throughout the crust

402   and upper mantle. Earth curvature will need to be considered when applying this method to a

403   larger spatial scale.

404   Both the material model and stress model are available in the supplementary materials.

5 Discussion and Conclusions

406   We jointly inverted surface-wave dispersion, gravity, and local travel time observations

407   for a 3D elastic property model for the Oklahoma region. The material model can be further

improved with deep learning and transfer learning derived travel time observations (Chai et al., 2020). Utilizing the 3D material model, a model of the 3D stress tensor field for Oklahoma was computed by considering both gravitational and tectonic contributions. A model that includes both gravitational and tectonic components of the stress field fits observed stress indicators better than the tectonic component alone, indicating that the gravitational component helps to explain small-scale variations in principal stress orientations. We used observed stress indicators and faulting types to constrain the tectonic force orientation and magnitude equivalent. Our preferred model has a tectonic force orientation of N82°E and explains well the stress observations and the faulting types. An equivalent stress magnitude near 123 MPa (shortening of 3965 m) fits the stress observations and the faulting types better than other magnitudes. This corresponds to a deviatoric shear stress of 10-30 MPa on optimally oriented faults. The stress field in the upper 5 km due to gravitational body forces has a comparable magnitude to the tectonic-driven stress field and the modeled stress field in the Oklahoma region has significant spatial variations.

Our results demonstrate that a reliable 3D stress field for the upper crust can be computed using a 3D material model and stress observations. When previous localized stress orientation measurements and focal mechanisms are known, the orientation and magnitude of the regional tectonic forces can be constrained through stress modeling. 3D stress modeling has significant advantages over traditional methods (e.g., interpolation, extrapolation) including the ability to obtain stress magnitudes and the ability to use measurements away from boreholes and earthquake focal mechanisms. As small-scale stress variations may favor or oppose future deformation, our technique can also help with subsurface engineering problems and natural hazards. Though our model closely recovers most available stress indicators, the stress tensor continues to be a difficult property to validate, which could be done with new observations.

453   DOE Public Access Plan (http://energy.gov/downloads/doe-public-access-plan). The authors

454   declare that they have no conflict of interest.

455   **References**

456   Alt, R. C., & Zoback, M. D. (2017). In Situ Stress and Active Faulting in Oklahoma. *Bulletin of*

457   *the Seismological Society of America*, *107*(1), 216–228. https://doi.org/10.1785/0120160156

458   Balmino, G., Vales, N., Bonvalot, S., & Briais, A. (2012). Spherical harmonic modelling to ultra-

459   high degree of Bouguer and isostatic anomalies. *Journal of Geodesy*, *86*(7), 499–520.

460   https://doi.org/10.1007/s00190-011-0533-4

461   Beyreuther, M., Barsch, R., Krischer, L., Megies, T., Behr, Y., & Wassermann, J. (2010). ObsPy:

462   A Python Toolbox for Seismology. *Seismological Research Letters*, *81*(3), 530–533.

463   https://doi.org/10.1785/gssrl.81.3.530

464   Chai, C. (2017). *Multi-Objective Geophysical Inversion for Earth Structure and Earthquake*

465   *Parameters*. The Pennsylvania State University. Retrieved from

466   https://search.proquest.com/docview/1922659974

467   Chai, C., Ammon, C. J., Maceira, M., & Herrmann, R. B. (2015). Inverting interpolated receiver

468   functions with surface wave dispersion and gravity: Application to the western U.S. and

469   adjacent Canada and Mexico. *Geophysical Research Letters*, *42*(11), 4359–4366.

470   https://doi.org/10.1002/2015GL063733

471   Chai, C., Ammon, C. J., Maceira, M., & Herrmann, R. B. (2018). Interactive Visualization of

472   Complex Seismic Data and Models Using Bokeh. *Seismological Research Letters*, *89*(2A),

473   668–676. https://doi.org/10.1785/0220170132

474   Chai, C., Maceira, M., Santos-Villalobos, H. J., Venkatakrishnan, S. V., Schoenball, M., Zhu,

475   W., et al. (2020). Using a Deep Neural Network and Transfer Learning to Bridge Scales for

476   Seismic Phase Picking. *Geophysical Research Letters*, *47*(16), e2020GL088651.

477   https://doi.org/10.1029/2020GL088651

478   Dziewonski, A. M., Chou, T.-A., & Woodhouse, J. H. (1981). Determination of earthquake

479   source parameters from waveform data for studies of global and regional seismicity.

480   *Journal of Geophysical Research: Solid Earth*, *86*(B4), 2825–2852.

481   https://doi.org/10.1029/JB086iB04p02825

482   Evanzia, D., Pulliam, J., Ainsworth, R., Gurrola, H., & Pratt, K. (2014). Seismic Vp & Vs

483   tomography of Texas & Oklahoma with a focus on the Gulf Coast margin. *Earth and*

484   *Planetary Science Letters*, *402*, 148–156. https://doi.org/10.1016/j.epsl.2013.12.027

485   Fleitout, L., & Froidevaux, C. (1982). Tectonics and topography for a lithosphere containing

486   density heterogeneities. *Tectonics*, *1*(1), 21–56. https://doi.org/10.1029/TC001i001p00021

487   Flesch, L. M., Holt, W. E., Haines, A. J., & Shen-Tu, B. (2000). Dynamics of the Pacific-North

488   American Plate Boundary in the Western United States. *Science*, *287*(5454), 834–836.

489   https://doi.org/10.1126/science.287.5454.834

490   Flesch, L. M., Holt, W. E., Haines, A. J., Wen, L., & Shen-Tu, B. (2007). The dynamics of

491   western North America: stress magnitudes and the relative role of gravitational potential

492   energy, plate interaction at the boundary and basal tractions. *Geophysical Journal*

493   *International*, *169*(3), 866–896. https://doi.org/10.1111/j.1365-246X.2007.03274.x

494   Forte, A. M., Mitrovica, J. X., Moucha, R., Simmons, N. A., & Grand, S. P. (2007). Descent of

495   the ancient Farallon slab drives localized mantle flow below the New Madrid seismic zone.

496   *Geophysical Research Letters*, *34*(4), L04308. https://doi.org/10.1029/2006GL027895

497   Ghosh, A., Becker, T. W., & Humphreys, E. D. (2013). Dynamics of the North American

498   continent. *Geophysical Journal International*, *194*(2), 651–669.

499   https://doi.org/10.1093/gji/ggt151

500 Ghosh, A., Holt, W. E., & Bahadori, A. (2019). Role of large-scale tectonic forces in intraplate

501   earthquakes of central and eastern North America. *Geochemistry, Geophysics, Geosystems*,

502   *20*(4), 2134–2156. https://doi.org/10.1029/2018GC008060

503 Gilbert, M. C. (1983). Timing and chemistry of igneous events associated with the Southern

504   Oklahoma Aulacogen. *Tectonophysics*, *94*(1–4), 439–455. https://doi.org/10.1016/0040-

505   1951(83)90028-8

506 Hardebeck, J. L., & Okada, T. (2018). Temporal stress changes caused by earthquakes: a review.

507   *Journal of Geophysical Research: Solid Earth*, *123*(2), 1350–1365.

508   https://doi.org/10.1002/2017JB014617

509 Heidbach, O., Reinecker, J., Tingay, M., Müller, B., Sperner, B., Fuchs, K., & Wenzel, F.

510   (2007). Plate boundary forces are not enough: Second- and third-order stress patterns

511   highlighted in the World Stress Map database. *Tectonics*, *26*(6), TC6014.

512   https://doi.org/10.1029/2007TC002133

513 Heidbach, O., Tingay, M., Barth, A., Reinecker, J., Kurfeß, D., & Müller, B. (2010). Global

514   crustal stress pattern based on the World Stress Map database release 2008. *Tectonophysics*,

515   *482*(1–4), 3–15. https://doi.org/10.1016/j.tecto.2009.07.023

516 Heidbach, O., Rajabi, M., Cui, X., Fuchs, K., Müller, B., Reinecker, J., et al. (2018). The World

517   Stress Map database release 2016: Crustal stress pattern across scales. *Tectonophysics*, *744*,

518   484–498. https://doi.org/10.1016/j.tecto.2018.07.007

519 Herrmann, R. B., Benz, H. M., & Ammon, C. J. (2016). Mapping Love/Rayleigh phase/group

520   velocity dispersion between 2 and 100 seconds in North America using ambient noise cross-

521   correlations and earthquake observations (abs). *Seismological Research Letters*, *87*(2B),

522   546.

523   Hsu, Y.-J., Rivera, L., Wu, Y.-M., Chang, C.-H., & Kanamori, H. (2010). Spatial heterogeneity

524   of tectonic stress and friction in the crust: new evidence from earthquake focal mechanisms

525   in Taiwan. *Geophysical Journal International*, *182*(1), 329–342.

526   https://doi.org/10.1111/j.1365-246X.2010.04609.x

527   Humphreys, E. D., & Coblentz, D. D. (2007). North American dynamics and western U.S.

528   tectonics. *Reviews of Geophysics*, *45*(3), 1–30. https://doi.org/10.1029/2005RG000181

529   Iio, Y., Yoneda, I., Sawada, M., Miura, T., Katao, H., Takada, Y., et al. (2017). Which is

530   heterogeneous, stress or strength? An estimation from high-density seismic observations.

531   *Earth, Planets and Space*, *69*(1), 144. https://doi.org/10.1186/s40623-017-0730-3

532   Isken, M. P., & Mooney, W. D. (2017). Relocated Hypocenters and Structural Analysis from

533   Waveform Modeling of Aftershocks from the 2011 Prague, Oklahoma, Earthquake

534   Sequence. *Bulletin of the Seismological Society of America*, *107*(2), 553–562.

535   https://doi.org/10.1785/0120160150

536   Johnson, K. (2008). *Geologic History of Oklahoma*. *Oklahoma Geological Survey*.

537   Laske, G., Masters, G., Ma, Z., Pasyanos, M. E., & Livermore, L. (2013). Update on CRUST1.0:

538   A 1-degree Global Model of Earth's Crust. *Geophys. Res. Abstracts*.

539   Levandowski, W., Boyd, O. S., & Ramirez-Guzmán, L. (2016). Dense lower crust elevates long-

540   term earthquake rates in the New Madrid seismic zone. *Geophysical Research Letters*,

541   *43*(16), 8499–8510. https://doi.org/10.1002/2016GL070175

542   Levandowski, W., Herrmann, R. B., Briggs, R., Boyd, O., & Gold, R. (2018). An updated stress

543   map of the continental United States reveals heterogeneous intraplate stress. *Nature*

544   *Geoscience*, *11*(6), 433–437. https://doi.org/10.1038/s41561-018-0120-x

545   Lin, H., Oh, J., Masoumi, H., Canbulat, I., Zhang, C., & Dou, L. (2018). A Review of In Situ

546   Stress Measurement Techniques. In *Proceedings of the 18th Coal Operators' Conference*

547   (pp. 95–102). Mining Engineering, University of Wollongong.

548   Liu, J., Ding, W., Yang, H., Wang, R., Yin, S., Li, A., & Fu, F. (2017). 3D geomechanical

549   modeling and numerical simulation of in-situ stress fields in shale reservoirs: A case study

550   of the lower Cambrian Niutitang formation in the Cen'gong block, South China.

551   *Tectonophysics*, *712–713*, 663–683. https://doi.org/10.1016/j.tecto.2017.06.030

552   Ljunggren, C., Chang, Y., Janson, T., & Christiansson, R. (2003). An overview of rock stress

553   measurement methods. *International Journal of Rock Mechanics and Mining Sciences*,

554   *40*(7–8), 975–989. https://doi.org/10.1016/j.ijrmms.2003.07.003

555   Lund Snee, J.-E., & Zoback, M. D. (2016). State of stress in Texas: Implications for induced

556   seismicity. *Geophysical Research Letters*, *43*(19), 10,208-10,214.

557   https://doi.org/10.1002/2016GL070974

558   Lund Snee, J.-E., & Zoback, M. D. (2020). Multiscale variations of the crustal stress field

559   throughout North America. *Nature Communications*, *11*(1), 1951.

560   https://doi.org/10.1038/s41467-020-15841-5

561   Maceira, M., & Ammon, C. J. (2009). Joint inversion of surface wave velocity and gravity

562   observations and its application to central Asian basins shear velocity structure. *Journal of*

563   *Geophysical Research*, *114*(B2), B02314. https://doi.org/10.1029/2007JB005157

564   Martínez-Garzón, P., Bohnhoff, M., Kwiatek, G., & Dresen, G. (2013). Stress tensor changes

565   related to fluid injection at The Geysers geothermal field, California. *Geophysical Research*

566   *Letters*, *40*(11), 2596–2601. https://doi.org/10.1002/grl.50438

567   McGarr, A., & Gay, N. C. (1978). State of stress in the Earth's crust. *Annual Review of Earth*

568   *and Planetary Sciences*, *6*(1), 405–436.

569   McNamara, D. E., Benz, H. M., Herrmann, R. B., Bergman, E. A., Earle, P., Holland, A., et al.

570   (2015). Earthquake hypocenters and focal mechanisms in central Oklahoma reveal a

571   complex system of reactivated subsurface strike-slip faulting. *Geophysical Research*

572   *Letters*, *42*(8), 2742–2749. https://doi.org/10.1002/2014GL062730

573   Nussbaum, C., Guglielmi, Y., Jaeggi, D., Bossart, P., & others. (2017). Estimation of the stress

574   tensor across a stimulated fault zone in the Opalinus Clay, Mont Terri Rock Laboratory. In

575   *ISRM Progressive Rock Failure Conference*.

576   Pedregosa, F., Varoquaux, G., Gramfort, A., Michel, V., Thirion, B., Grisel, O., et al. (2011).

577   Scikit-learn: Machine Learning in Python. *Journal of Machine Learning Research*, *12*,

578   2825–2830.

579   Porter, R., Liu, Y., & Holt, W. E. (2016). Lithospheric records of orogeny within the continental

580   U.S. *Geophysical Research Letters*, *43*(1), 144–153. https://doi.org/10.1002/2015GL066950

581   Reiter, K., & Heidbach, O. (2014). 3-D geomechanical–numerical model of the contemporary

582   crustal stress state in the Alberta Basin (Canada). *Solid Earth*, *5*(2), 1123–1149.

583   https://doi.org/10.5194/se-5-1123-2014

584   Richardson, R. M., & Reding, L. M. (1991). North American plate dynamics. *Journal of*

585   *Geophysical Research*, *96*(B7), 12201. https://doi.org/10.1029/91JB00958

586   Richardson, R. M., Solomon, S. C., & Sleep, N. H. (1979). Tectonic stress in the plates. *Reviews*

587   *of Geophysics*, *17*(5), 981–1019. https://doi.org/10.1029/RG017i005p00981

588   Rivera, L., & Kanamori, H. (2002). Spatial heterogeneity of tectonic stress and friction in the

589   crust. *Geophysical Research Letters*, *29*(6), 12-1-12–4.

590   https://doi.org/10.1029/2001GL013803

Schmandt, B., Lin, F.-C., & Karlstrom, K. E. (2015). Distinct crustal isostasy trends east and west of the Rocky Mountain Front. *Geophysical Research Letters*, *42*(23), 10,290-10,298. https://doi.org/10.1002/2015GL066593

Schoenball, M., & Davatzes, N. C. (2017). Quantifying the heterogeneity of the tectonic stress field using borehole data. *Journal of Geophysical Research: Solid Earth*, *122*(8), 6737–6756. https://doi.org/10.1002/2017JB014370

Segall, P. (1989). Earthquakes triggered by fluid extraction. *Geology*, *17*(10), 942–946. https://doi.org/10.1130/0091-7613(1989)017<0942:ETBFE>2.3.CO;2

Shearer, P. M. (2009). *Introduction to Seismology*. *Introduction to Seismology*. Cambridge: Cambridge University Press. https://doi.org/10.1017/CBO9780511841552

Shen, W., & Ritzwoller, M. H. (2016). Crustal and uppermost mantle structure beneath the United States. *Journal of Geophysical Research: Solid Earth*, *121*(6), 4306–4342. https://doi.org/10.1002/2016JB012887

Simpson, R. W. (1997). Quantifying Anderson's fault types. *Journal of Geophysical Research: Solid Earth*, *102*(B8), 17909–17919. https://doi.org/10.1029/97JB01274

Syracuse, E. M., Maceira, M., Zhang, H., & Thurber, C. H. (2015). Seismicity and structure of Akutan and Makushin Volcanoes, Alaska, using joint body and surface wave tomography. *Journal of Geophysical Research: Solid Earth*, *120*(2), 1036–1052. https://doi.org/10.1002/2014JB011616

Syracuse, E. M., Maceira, M., Prieto, G. A., Zhang, H., & Ammon, C. J. (2016). Multiple plates subducting beneath Colombia, as illuminated by seismicity and velocity from the joint inversion of seismic and gravity data. *Earth and Planetary Science Letters*, *444*, 139–149. https://doi.org/10.1016/j.epsl.2016.03.050

614 Syracuse, E. M., Zhang, H., & Maceira, M. (2017). Joint inversion of seismic and gravity data

615   for imaging seismic velocity structure of the crust and upper mantle beneath Utah, United

616   States. *Tectonophysics*, *718*, 105–117. https://doi.org/10.1016/j.tecto.2017.07.005

617 Waldhauser, F. (2000). A double-difference earthquake location algorithm: method and

618   application to the Northern Hayward Fault, California. *Bulletin of the Seismological Society*

619   *of America*, *90*(6), 1353–1368. https://doi.org/10.1785/0120000006

620 Walsh, F. R., & Zoback, M. D. (2016). Probabilistic assessment of potential fault slip related to

621   injection-induced earthquakes: Application to north-central Oklahoma, USA. *Geology*,

622   *44*(12), 991–994. https://doi.org/10.1130/G38275.1

623 Wessel, P., Smith, W. H. F., Scharroo, R., Luis, J., & Wobbe, F. (2013). Generic Mapping Tools:

624   improved version released. *Eos, Transactions American Geophysical Union*, *94*(45), 409–

625   410. https://doi.org/10.1002/2013EO450001

626 Wesson, R. L., & Boyd, O. S. (2007). Stress before and after the 2002 Denali fault earthquake.

627   *Geophysical Research Letters*, *34*(7), L07303. https://doi.org/10.1029/2007GL029189

628 Zhang, H., & Thurber, C. (2003). Double-difference tomography: the method and its application

629   to the Hayward Fault, California. *Bulletin of the Seismological Society of America*, *93*(5),

630   1875–1889. https://doi.org/10.1785/0120020190

631 Zhang, H., & Thurber, C. (2006). Development and Applications of Double-difference Seismic

632   Tomography. *Pure and Applied Geophysics*, *163*(2–3), 373–403.

633   https://doi.org/10.1007/s00024-005-0021-y

634 Zoback, M. D., Paul, P., & Lucier, A. (2010). Utilizing observations of borehole failure in

635   deviated wellbores to constrain the full stress tensor in deep wells and mines: application to

636   two complex case studies. In *International Symposium on in-situ Rock Stress, Beijing,*

637   *China* (pp. 69–76).

638   Zoback, M. L., & Magee, M. (1991). Stress magnitudes in the crust: constraints from stress

639   orientation and relative magnitude data. *Philosophical Transactions of the Royal Society of*

640   *London. Series A: Physical and Engineering Sciences*, *337*(1645), 181–194.

641   https://doi.org/10.1098/rsta.1991.0115

642   Zoback, M. Lou. (1992). Stress field constraints on intraplate seismicity in eastern North

643   America. *Journal of Geophysical Research*, *97*(B8), 11761.

644   https://doi.org/10.1029/92JB00221

645   Zoback, M. Lou, & Zoback, M. (1980). State of stress in the conterminous United States.

646   *Journal of Geophysical Research: Solid Earth*, *85*(B11), 6113–6156.

647   https://doi.org/10.1029/JB085iB11p06113

648